Applied Surface Science 685 (2025) 162059

Contents lists available at ScienceDirect

Applied Surface Science

journal homepage: www.elsevier.com/locate/apsusc

Full Length Article

Tunable optical anisotropy and multiplied-enhancement birefringence of α-MoO_3 under in-plane strain by first-principles calculations

Zhengfeng Guo [a,b], Jingbo Sun [b], Ji Zhou [b], Honggang Gu [a,c,*], Shiyuan Liu [a,c,*]

[a] School of Mechanical Science and Engineering, Huazhong University of Science and Technology, Wuhan, Hubei 430074, China
[b] State Key Laboratory of New Ceramics and Fine Processing, School of Materials Science and Engineering, Tsinghua University, Beijing 100084, China
[c] Optics Valley Laboratory, Hubei 430074, China

ARTICLE INFO

Keywords:
α-MoO_3
Birefringent materials
Optical anisotropy
Strain engineering
First-principles calculations

ABSTRACT

Strain offers a degree of freedom to realize the adjustability and enhancement of optical anisotropy. Herein, we theoretically and comprehensively investigate the tunable optical anisotropy and multiplied-enhancement birefringence of α-MoO_3 under in-plane strain, and further reveal the strain modulation mechanism by band structure and dipole moment of strained α-MoO_3. We find the optical anisotropy of strained α-MoO_3 is highly tunable. The starting operation wavelength λ_s and the birefringence Δn descend under *a*-axis strain and ascend under *c*-axis strain, and under biaxial strain they fall within the range of their counterparts under *a*-axis and *c*-axis strain. We also find the $|\Delta n|_{max}$ is 0.288 @ 509 nm, whose percent ratio to that of unstrained α-MoO_3 is as high as 436%. Besides, the λ_s is extended to approach the UV region by the *c*-axis compressive strain. The band structure results indicate bandgap E_g plays a dominate role in determining the strain-modulating λ_s, and the enhancement of Δn of strained α-MoO_3 originates from the contribution of ionic dipole moment. The strained α-MoO_3 can make device tunable and vastly improve the its performance, and the proposed calculation method and strain modulation mechanism in this paper can be extended to other optically anisotropic and birefringent materials.

1. Introduction

As a representative member of low-symmetry materials, the lattice structure of α-MoO_3 belongs to orthorhombic system, whose space group is *Pbnm* (No. 62) [1,2]. As a result, the low-symmetry structure brings α-MoO_3 optical anisotropy [3–5]. Optical anisotropy adds the research dimension and physics that the isotropy materials do not possess, such as birefringence Δn [6,7] as well as dichroism Δk [8,9]. Also, optical anisotropy provides an extra and unique opportunity to construct polarization-related devices based on α-MoO_3, such as polarizer [10], polarization converters [11], and etc. Moreover, α-MoO_3 owns a wide bandgap E_g like other transition metal oxides [12,13], which is 3.128 eV calculated in this paper and in accord with the experimental data [14,15] and other theoretically calculated results [16,17]. Such wide bandgap contributes to the fall and even absence of absorption in visible and infrared region. Accordingly, α-MoO_3 potentially stands a chance of being a visible and infrared birefringent material, which is due to the fact that the α-MoO_3's absorption drops and even vanishes within such region and the optical anisotropy still exists. For the birefringent material, the birefringence Δn is generally employed to quantify and compare the magnitude of optical anisotropy. The commercial birefringent materials such as quartz and MgF_2 are widely-applied. Their birefringence Δn, however, are relatively low ($\Delta n_{quartz} = 0.009$ [18] and $\Delta n_{MgF2} = 0.011$ [19] in visible and NIR region). More recently, the low-symmetry materials like α-MoO_3 are regarded as a promising candidate to replace the commercial birefringent materials because of their greatly optical anisotropy. The calculated in-plane Δn of strain-free α-MoO_3 in this paper is only about 0.1, which also accords with experimental result [20,21]. Although such Δn of strain-free α-MoO_3 is about one order of magnitude higher than those of quartz and MgF_2, there still remains much room for enhancement of Δn to obtain high-performance of corresponding devices, such as waveplates [22,23], Dyakonov surface waves devices [24,25]. Huge Δn means the thickness of waveplates *d* can be immensely decreased as the phase retardance δ is in proportion to Δn and *d* [23], and the specific function of waveplates determines δ (For instance, the δ of quarter-waveplate is 90° [26]). The reduction of

* Corresponding authors at: Nanoscale and Optical Metrology Center, School of Mechanical Science and Engineering, Huazhong University of Science and Technology, 1037 Luoyu Road, Wuhan, Hubei 430074, China.
E-mail addresses: hongganggu@hust.edu.cn (H. Gu), shyliu@hust.edu.cn (S. Liu).

https://doi.org/10.1016/j.apsusc.2024.162059
Received 30 September 2024; Received in revised form 30 November 2024; Accepted 8 December 2024
Available online 9 December 2024

waveplate thickness helps to realize the miniaturization of devices, and thus can be integrated into corresponding miniature optical instruments. For Dyakonov surface waves devices, the main bottleneck that needs to break through in this research field is the limited propagation angular range $\Delta\theta$ while the giant Δn brings the expansion of $\Delta\theta$ [27]. Therefore, the birefringence Δn is required to be further enhanced. Besides, if the optical anisotropy of α-MoO_3 becomes tunable under external stimulation, the corresponding devices based on α-MoO_3 are capable of being adjustable.

Strain offers a degree of freedom to realize the adjustability and enhancement of material properties. Despite the fact that there are many other external stimulations like temperature [10,28], pressure [29,30], electric or magnetic field [31–33], and so on, which provide a helpful and useful way to tune the properties of materials in optics and electronics. Stress, however, is relatively convenient to experimentally realize with diverse method, such as using flexible or patterned substrates [34,35], lattice mismatch [36,37], AFM tip [38,39] and etc. Besides, instead of complicate calculation parameter settings of other external field modulation, the implementation of strain modulation in first-principles calculations is also facile as one just needs to change the lattice constant of material under the corresponding strain. Apart from convenience and diversity of implementation method, the finesse of strain modulation is also distinguished from other modulation method as one can apply stress along different directions with tunable magnitude. For example, the stress applied in materials can be uniaxial or biaxial or even along an arbitrary direction if necessary, which is pretty vital for anisotropic materials. Also, the magnitude of strain, can be classified into tensile or compressive strain, makes the modulation fine and tunable. Moreover, a wide variety of material properties can be regulated by the strain [40,41], especially the optical and electronic properties. In optics, strain is capable of modulating the behavior of photoluminescence, absorption, and so on [42–44], and the electronic bandgap is tunable under strain [45,46]. For α-MoO_3, literature reported that the electronic band structure can be regulated by biaxial strain [47], indicating the properties of α-MoO_3 is sensitive to the stress. Nevertheless, as far as we know, there are only a small minority of theoretical researches quantitatively investigating the optical anisotropy under strain. Besides, theoretical researchers tend to display the results under strain, such as anisotropic complex refractive indices, anisotropic absorption coefficients, and etc., lacking of further analysis and discussion and revealing the mechanism behind, let alone experimental scientists studying the variation of birefringence under strain.

In this work, with the help of first-principles calculations, we comprehensively investigate the tunable optical anisotropy and multiplied-enhancement birefringence of α-MoO_3 under in-plane strain, and further reveal the strain modulation mechanism by calculating band structure and dipole moment of strained α-MoO_3. The selection of α-MoO_3 is because of not only its optical anisotropy caused by the low-symmetry structure but also the wide bandgap E_g, making α-MoO_3 a promising candidate of birefringent materials. The strain is selected to further modulate and enhance the birefringence Δn of α-MoO_3 owing to its facile implementation and fineness with desired directions and magnitude. Firstly, we study the anisotropic properties of unstrained α-MoO_3, including band structure as well as the derived electronic anisotropy and optical anisotropy. After confirming the birefringent material characteristics of α-MoO_3, the in-plane strain, including *a*-axis, *c*-axis, and biaxial compressive and tensile strain, is applied to further modulate optical anisotropy and improve birefringent performance parameters. To understand the strain modulation effect on optically anisotropic and birefringent α-MoO_3, the band structure and dipole moment under in-plane strain are calculated.

2. Computational details

The optical and electronic properties of intrinsic and strained α-MoO_3 were calculated by the Vienna ab initio package (VASP) [48] with the Perdew-Burke-Ernzerhopf (PBE) functional [49] based on projector-augmented-wave (PAW) pseudopotentials. In the geometry optimization, the PBE and other different van der Waals (vdW) corrections, as listed in Table S1 of Supplementary Material, were used to find the optimized structure of α-MoO_3 with lowest percentage error with respect to the experimental data. In addition, the strained α-MoO_3 is only relaxed and optimized the positions of atoms instead of the lattice parameters. Apart from PBE functional, HSE06 hybrid functional [50] was also adopted to calculated the band structure and projected density of states (PDOS). To calculate the optical properties of unstrained and strained α-MoO_3, the independent particle approximation (IPA) method is utilized.

The convergence criterion for forces in structure relax was set to 0.01 eV/Å. After carefully checking, the cutoff energy and the Γ-centered Monkhorst–Pack **k**-point mesh were respectively fixed at 550 eV and $2 \times 7 \times 7$ to make sure convergence with a criterion for total energy less than 10^{-5} eV. See Supporting Note S1 as well as Fig. S1 for more details about reason for selecting cutoff energy of 550 eV and **k**-point mesh of $2 \times 7 \times 7$. To calculate the PDOS, a finer **k**-point mesh of $5 \times 17 \times 17$ (except $5 \times 19 \times 19$ for −10% in-plane strain) was utilized after convergence test. More details can be found in Supporting Note S2 and Fig. S2.

3. Results and discussion

3.1. Anisotropic and birefringent properties of unstrained α-MoO_3

Low-symmetry lattice structure and structure relax of α-MoO_3. Fig. 1a and b illustrates the lattice structure of α-MoO_3, where the octahedron, composed by one Molybdenum (Mo) atom and six Oxygen (O) atoms, shares its corners and edges with other octahedrons respectively along the *c* axis and *a* axis. The different arrangements of the Mo-O octahedron along the *c* axis and *a* axis give rise to the in-plane anisotropy of α-MoO_3. As a typical vdW material, the layered structure arranges along the *b* axis of α-MoO_3, bonded by the vdW forces rather than the covalent interactions in the *a*-*c* plane [3]. The different interactions in the *a*-*c* plane and along the *b* axis of α-MoO_3 will lead to the out-of-plane anisotropy.

Before calculating the intrinsic properties of α-MoO_3, the lattice structure adopted from experimental data needs to be relaxed by PBE functional and different vdW corrections. As shown in Table S1, although the in-plane lattice constants *a* and *c* relaxed by PBE functional quite approach to those of experimental data, the out-of-plane lattice constant *b* much larger than the experimental one with a percentage error of 14.62%. As is known, PBE functional is not good at dealing with the optimization lattice constant of the crystal axis along which the vdW interactions exist [7,51]. Therefore, we carried out the geometry optimization via different vdW corrections to obtain the nearest results compared with the experimental data. Among the vdW corrections listed in Table S1, it is found that the lattice constant *b* optimized by DFT (PBE)-D2 [52] possesses the lowest percentage error with respect to the experimental data. Besides, the lattice constants *a* and *c* are also rather close to the experimental data. As a result, the lattice structure relaxed by the DFT(PBE)-D2 vdW correction was selected to further calculate the intrinsic properties of α-MoO_3.

Band structure and anisotropically electronic properties of unstrained α-MoO_3. Respectively illustrated in Figs. S3 and S4, we firstly calculated the band structure as well as PDOS of α-MoO_3 by using PBE functional method. More details can be found in Supporting Note S3. The calculated bandgap energy E_g by PBE method, however, is far from the experimental data [14,15]. Hence, we further calculated the band structure of α-MoO_3, showing in Fig. 1c, with the help of HSE06 hybrid functional method. Similar to the case calculated by PBE functional, the conduction band minimum (CBM) and the valence band maximum (VBM) are still at the Γ point and the T point respectively, which means the α-MoO_3 is still an indirect bandgap semiconductor. Differently, the

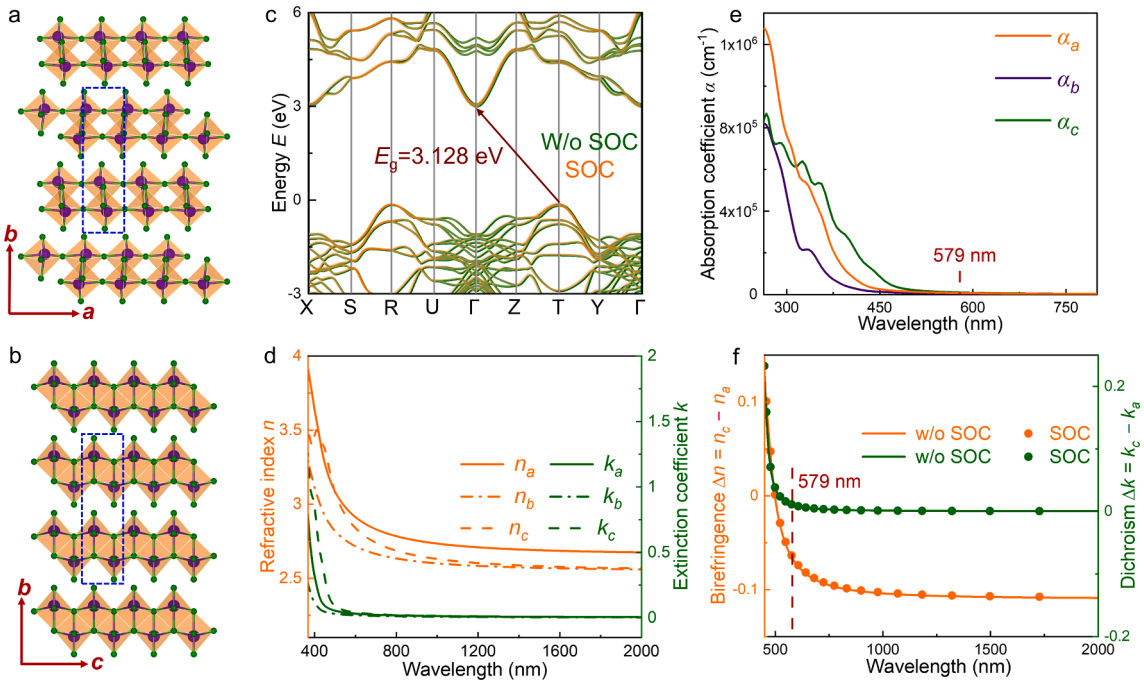

Fig. 1. Lattice structure of α-MoO_3 along the *c* axis (a) and (b) the *a* axis, where violet and green balls respectively represent Molybdenum (Mo) and Oxygen (O) atoms and the dashed blue boxes represent the unit cell. Electronic band structure of α-MoO_3 calculated by hybrid functional of HSE06 method without (w/o) and with considering spin–orbit coupling (SOC) effect (c). Anisotropic complex refractive indices (d) and anisotropic absorption coefficients α along three crystal axes (e) as well as derived in-plane birefringence Δn and dichroism Δk (f).

E_{CBM} and the E_{VBM} are much larger than their counterparts calculated by the PBE functional, and they are respectively 2.988 and −0.140 eV. As a result, the bandgap energy E_g increases to 3.128 eV, which is much larger than that calculated by the PBE functional and in accord with the experimental data [14,15] as well as other theoretically calculated results [16,17]. Moreover, the spin–orbit coupling (SOC) effect have scarcely influence on E_{CBM} and E_{VBM} as well as derived E_g. Shown in both Fig. S3 and Fig. 1c, the spin orbit splitting phenomenon hardly to be observed [53,54] and the calculated band structure with and without SOC effect share almost the same shapes. Moreover, the SOC effect has no influence on the locations of VBM and CBM, and the energy differences of E_{CBM} and E_{VBM} between with and without considering SOC effect are both within several meV. Such tiny differences also bring about 1∼2 meV differences in E_g for both PBE and HSE06 methods. Accordingly, the SOC effect will not be taken into account in the following calculations on electronic property of strained α-MoO_3.

The anisotropically electronic property of α-MoO_3 can be revealed from the electronic band structure by calculating the anisotropic carrier effective masses. The effective masses m^* of electron and hole can be calculated from the second order derivative of the CBM and VBM respectively. Besides, for the low-symmetry materials, anisotropic effective masses can be obtained from different directions in brillouin zone (BZ). For bulk α-MoO_3, carrier effective mass along the *a*-axis can be obtained within Γ point to Z point while the *c*-axis carrier effective mass can be acquired within Γ point to Y point. Therefore, the anisotropic effective masses of electron and hole along the *a*-axis and the *c*-axis can be represented as [55,56]

$$m^*_{i,j} = \frac{\partial^2 E_i}{\partial k_j^2} \ (i = e,\ h;\ j = a,\ c) \tag{1}$$

where the subscripts i (= e, h) and j (= a, c) represent the carrier type (electron and hole) and the crystal axes (*a*-axis and *c*-axis) of α-MoO_3, respectively. As shown in Table 1, both effective mass of the electron m^*_e and effective mass of the hole m^*_h demonstrate quite obvious anisotropy since the m^*_e and the m^*_h along the *a*-axis exhibit much differences from those along the *c*-axis. Specifically, for the electron, the effective mass along *c*-axis $m^*_{e,c}$ is about 1.7 times as the effective mass along *a*-axis $m^*_{e,a}$ while the ratio of effective mass of hole along *c*-axis $m^*_{h,c}$ to effective mass of hole along *a*-axis $m^*_{h,a}$ approaches as large as 1.2.

Table 1
Theoretical calculations on the effective mass m^* of electron and hole along the *a* axis and the *c* axis of α-MoO_3.

Directions	$m^*_e[m_0]$[a]	$m^*_h[m_0]$[a]
Along *a* axis	0.68	1.45
Along *c* axis	1.17	1.76

[a] The subscript *e* and *h* respectively represent the electron and the hole, and m_0 is the mass of free electron, which is equal to 9.11 × 10^{-31} kg.

Apart from the anisotropy of effective masses, we also calculated the carrier mobility μ to further demonstrate the anisotropically electronic property of α-MoO3, listed in Table S2. It is found that *c*-axis mobility of electron and hole ($\mu_{e,c}$ and $\mu_{h,c}$) are respectively about 7 and 7.5 times as high as those along the *a*-axis ($\mu_{e,a}$ and $\mu_{h,a}$). We also investigated anisotropic the mobility doped with different concentration of electron and hole with the help of AMSET method [57,58]. Please see Supporting Note S4 and Fig. S5 for more details.

Anisotropically optical and birefringent properties of unstrained α-MoO3. The anisotropically electronic properties generates the anisotropic electric polarizations, especially the anisotropic electric polarization in the ultraviolet (UV) and visible region, ultimately resulting in the anisotropic dielectric functions [56,59]. Illustrated in Fig. S6, the dielectric functions ε of α-MoO_3 is highly anisotropic. To be specific, the real part of dielectric functions ε_r demonstrate remarkable discrepancies along three crystal axes. Despite the fact that there is no absorption under the bandgap energy E_g and thus no difference beyond the corresponding wavelength, the imaginary part of dielectric functions ε_i along three crystal axes emerge to be highly different from each other near UV region. Such anisotropic dielectric functions ($\varepsilon_j = \varepsilon_{r,j} + i\varepsilon_{i,j}, j =$ *a*, *b*, *c*) means the anisotropic complex refractive indices ($N_j = n_j + ik_j, j$

$= a, b, c$) in Fig. 1d since anisotropic dielectric functions can be directly converted from anisotropic complex refractive indices, according to following equations [9,60]

$$\varepsilon_j = N_j^2,\ j = a,\ b,\ c; \tag{2a}$$

$$\varepsilon_{r,j} + i\varepsilon_{i,j} = (n_j + ik_j)^2,\ j = a,\ b,\ c. \tag{2b}$$

After deformations and simplifications, the Eq. (2) above can be further derived as

$$n_j = \sqrt{\frac{\varepsilon_{r,j} + \sqrt{\varepsilon_{r,j}^2 + \varepsilon_{i,j}^2}}{2}},\ j = a,\ b,\ c; \tag{3a}$$

$$k_j = \sqrt{\frac{-\varepsilon_{r,j} + \sqrt{\varepsilon_{r,j}^2 + \varepsilon_{i,j}^2}}{2}},\ j = a,\ b,\ c. \tag{3b}$$

In Eq. (3), n_j and k_j ($j = a, b, c$) are respectively the refractive index and the extinction coefficient along the a, b, and c axis of α-MoO_3.

More excitingly, α-MoO_3 is a typically birefringent materials, which means all the extinction coefficients k_j ($j = a, b, c$) along three axes drop to zero in visible and near-infrared (NIR) region while the refractive indices n_j ($j = a, b, c$) along the a, b, and c axis exhibit giant differences within the same region. For birefringent materials, two main performance parameters are the most important, and one is the starting operation wavelength λ_s and the other is the birefringence Δn.

The birefringent materials are required to be fairly low-loss or even lossless within its operation wavelength. Therefore, the starting operation wavelength λ_s is defined to quantify the operation wavelength region, which means the birefringent materials work well beyond the starting operation wavelength λ_s. Here, illustrated in Fig. 2e, we adopt the absorption coefficient α to define the starting operation wavelength λ_s, which can be calculated directly from the extinction coefficients k [9,60]

$$\alpha_j = \frac{4\pi k_j}{\lambda},\ j = a,\ b,\ c. \tag{4}$$

In consequence, according to the Eq. (4), α_j ($j = a, b, c$) along three axes share the same tendency with k_j ($j = a, b, c$), and they all gradually drop to zero in visible and NIR region and there is no longer existing any peak. Therefore, the starting operation wavelength λ_s can be defined as the wavelength corresponding to absorption coefficient α of 1×10^5 cm^{-1} that is fairly low-loss. For the intrinsic α-MoO_3, the starting operation wavelength λ_s is 579 nm, which is in the visible region.

The other significant performance parameter is the birefringence Δn which is defined as the difference value of refractive index n. Here, as is demonstrated in Fig. 1f, we calculated the difference value of in-plane refractive index n, *i.e.* birefringence Δn ($= n_c - n_a$), as well as the in-plane extinction coefficient k, *i.e.* dichroism Δk ($= k_c - k_a$). At the starting operation wavelength λ_s, the birefringence Δn is −0.066 while the dichroism Δk is only 0.012 at the same wavelength. The dichroism Δk approaches to zero in the NIR region while the absolute value of birefringence Δn gradually rise and.

maintain a relatively high level (*e.g.* $|\Delta n| = 0.105$ @ 1064 nm) in visible and NIR region. The calculated birefringence Δn agrees with the experimental reported results [20,21]. Also, the Δn and the Δk are scarcely influenced by the SOC effect since the calculated Δn and Δk considering the SOC effect are almost the same as those without considering the SOC effect. Accordingly, the SOC effect is ignored in the subsequent calculations on optical properties of strained α-MoO_3.

3.2. *Strain-tunable optical anisotropy and strain-enhanced birefringent performance of α-MoO_3*

The typically birefringent material α-MoO_3 possesses superior performance, which is because of not only the visible-region starting operation wavelength λ_s but also the relatively high birefringence Δn. We wonder if the birefringent performance of α-MoO_3 can be further tunable or even enhanced under strain? First of all, it is of rather necessity to investigate stability of the unstrained α-MoO_3, and the superior mechanical property of the unstrained α-MoO_3 is the foundation of stability of α-MoO_3 under in-plane strain. With the help of the first-principles, we calculated the elastic constants (Table S3) and the derived Young's modulus E as well as Poisson's ratio ν, and all of them indicate the superior mechanical property of the unstrained α-MoO_3. More details can be found in Supporting Note S5.We also discuss the stability of α-MoO_3 under in-plane strain, and the stress–strain curve is the first matter that needs to be considered and calculated to determine

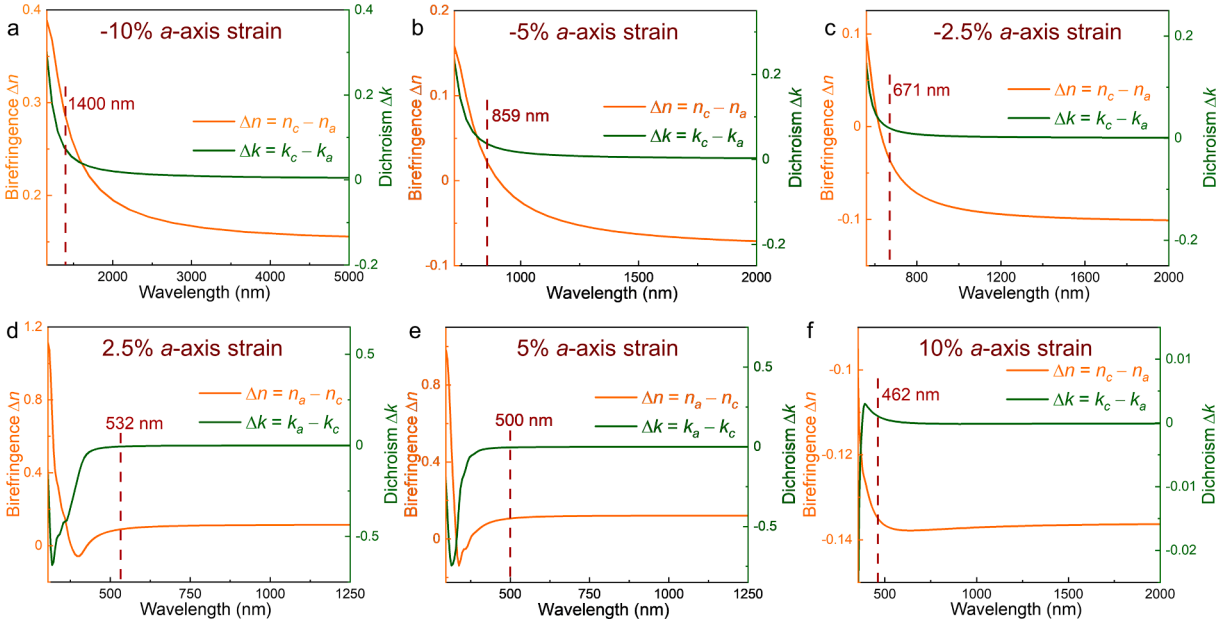

Fig. 2. The in-plane birefringence Δn as well as dichroism Δk under a-axis compressive strain (a~c) and the tensile strain (d~f), where the marked wavelength is the starting operation wavelength λ_s.

the appropriate strain range. As illustrated in Fig. S7a–c as well as Fig. S8a–c, the in-plane strain, including the *a*-axis, *c*-axis, and biaxial strain, are the most convenient to apply and also the most concerned about. Shown in Fig. S7d, the in-plane compressive stress maintain a linear relation with strain within a range of −10%, which shares the similar situation with the in-plane tensile strain within a range of 10% in Fig. S8d. The linear relation between stress and strain suggests that α-MoO_3 is recoverable and thus stable within this strain range [61,62] As a consequence, the −10%~10% in-plane strain is applied to α-MoO_3 to explore its effect on optical anisotropy. Here, the strain is denoted as $\Delta l/l_0$, where Δl and l_0 respectively represent the variations of lattice constants along in-plane axes (*a*-axis and *c*-axis) and the initial lattice constants without applying stress. Obviously, to apply in-plane stress is to change the in-plane lattice constants of α-MoO_3.

We first take the *a*-axis strain, displayed in Fig. 2, as a representative sample to probe into the strain-tunable optical anisotropy of α-MoO_3. Although the starting operation wavelength λ_s and the birefringence Δn alter under the varying strain, the α-MoO_3 still keeps the feature of birefringent materials. Specifically speaking, under the strain along the *a*-axis, the λ_s gradually decreases from 1400 nm to 462 nm as the strain changes from strongest compressive one (−10% *a*-axis strain) to the strongest tensile one (10% *a*-axis strain), illustrated in Fig. 3a. As summed in Table S4, the dichroism Δk also possess the same variation tendency as λ_s, which is from 0.074 to 0.001. The λ_s is defined as the wavelength of specific absorption coefficient α ($= 1 \times 10^5$ cm^{-1}), and thus to make α unchanged, according to Eq. (4), the Δk and the λ_s should keep the same variation tendency. Besides, as demonstrated in Fig. 3b and summed in Table S4, the Δn reduces gradually from 0.285 to −0.135 at the corresponding λ_s under the same variation of strain. One can see Figs. S9 and S10 for more details. Unfortunately, although the absolute value of birefringence $|\Delta n|$ under −10% *a*-axis strain is about 4.3 times as that of unstrained α-MoO_3, the λ_s is limited at the wavelength of 1400 nm in the NIR region. At the meantime, the λ_s is extended to the wavelength of 462 nm by applying 10% *a*-axis strain. However, the enhancement of $|\Delta n|$ under 10% *a*-axis strain is far less than that under −10% *a*-axis strain.

Thus, to obtain the excellent birefringent performance, *i.e.* extended λ_s and giant $|\Delta n|$, we further calculated the optical properties of α-MoO_3 under the *c*-axis compressive and tensile strain, respectively demonstrated in Figs. S11 and S12. Compared with the case under *a*-axis strain, the modulation range wavelength of λ_s is vastly reduced in Fig. 3a, which is from the wavelength of 509 nm to that of 781 nm. Besides, summed in Table S4, the *c*-axis compressive strain extends the λ_s to approach the UV region, instead of making λ_s red shift to NIR region like the *a*-axis compressive strain. Additionally, unlike the *a*-axis compressive strain, the absolute value of dichroism $|\Delta k|$ under *c*-axis compressive strain is extremely tiny, which is at level of thousandth shown in Table S4. Moreover, the Δn under *c*-axis strain, summed in Table S4 and illustrated in Fig. 3b, is also tunable, which is from −0.288 to 0.155 at the corresponding λ_s under *c*-axis strain from −10% to 10%. More excitingly, apart from the tunability, Δn also owns a nearly linear relation with the *c*-axis strain, shown in Fig. 3b. It is also found that the $|\Delta n|$ under −10% *c*-axis strain is a little higher than that under −10% *a*-axis strain. Differently and excitingly, the λ_s under −10% *c*-axis strain is extended to the wavelength of 509 nm rather than the NIR-region λ_s under −10% *a*-axis strain. The birefringent performance of α-MoO_3, consequently, can be further enhanced by applying −10% *c*-axis strain. In detail, compare to the unstrained α-MoO_3, the −10% *c*-axis strain makes λ_s blue shift for 70 nm to get close to the UV region. Meanwhile, the percent ratio of $|\Delta n|$ under the −10% *c*-axis strain to that of unstrained α-MoO_3 at its corresponding λ_s is as high as 436%. Additionally, $|\Delta k|$ under −10% *c*-axis strain at λ_s is only 0.005, which is 58.3% lower than that of unstrained α-MoO_3.

As is shown in Figs. S13 and S14, the in-plane biaxial strain were also calculated, and we find that both the λ_s and the Δn at the corresponding λ_s under in-plane biaxial strain, respectively displayed in Fig. 3a and b, are within the range of their counterparts under *a*-axis and *c*-axis strain. Applying the in-plane biaxial strain means to apply the same magnitude

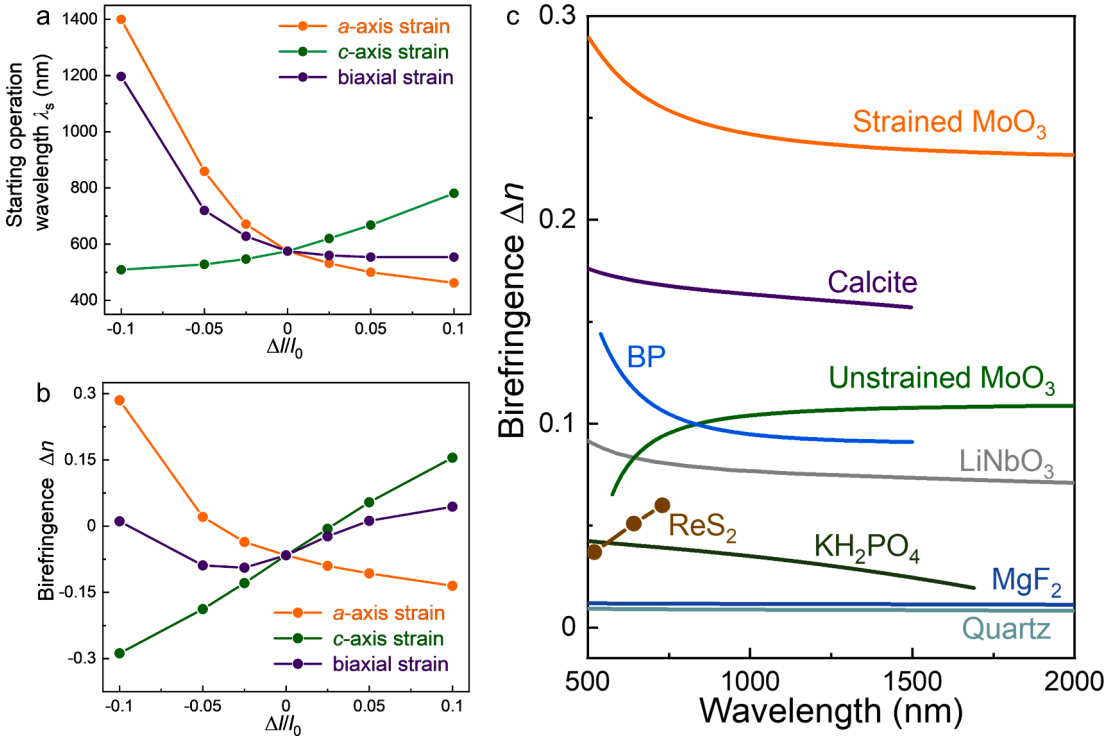

Fig. 3. The starting operation wavelength λ_s (a) and the birefringence Δn at the λ_s (b) under in-plane strain. Comparation of Δn of strained (−10% *c*-axis strain) and unstrained MoO_3 with other birefringent materials (quartz [18], MgF_2 [19], KH_2PO_4 [63], $LiNbO_3$ [64], and calcite [18]) and low-symmetry materials (ReS_2 [23] and black phosphorus, *i.e.* BP [65]) (c). For convenience of comparison, the Δn of strained and unstrained MoO_3 have been recalculated with the relation of $\Delta n = n_a - n_c$.

of *a*-axis and *c*-axis strain simultaneously, and thus the birefringent performance of α-MoO_3 will not exceed the scopes of the λ_s and the Δn under *a*-axis and *c*-axis strain.

As illustrated in Fig. S15, we also extracted the Δn at the wavelength of 1064 nm which is typical and widely used NIR wavelength [66,67]. Due to the fact that the λ_s under −10% *c*-axis strain as well as −10% biaxial strain is fairly larger than 1064 nm, the Δn under such strain can be ignored. Even so, Δn under in-plane strain at the wavelength of 1064 nm still display the similar trend with the Δn at the λ_s. More specifically, Δn under *a*-axis strain decreases with the strain rising from −10% to 10%. On the contrary, by applying the *c*-axis strain, Δn ascends with the increasement of the strain. Furthermore, Δn under *c*-axis strain also exhibits a pretty linear relation with strain with a maximum $|\Delta n|$ of 0.24 under −10% *c*-axis strain. For the biaxial strain, Δn still almost falls within the scope of those under *a*-axis and *c*-axis strain.

Shown in Fig. 3c, we also made a comparation of Δn of strained (−10% *c*-axis strain) and unstrained MoO_3 with other birefringent materials and low-symmetry materials. For birefringent materials like quartz [18] and MgF_2 [19], despite wide application, their Δn are only about 0.009 and 0.011 in visible and NIR region respectively, which is about one order of magnitude lower than that of unstrained MoO_3 in NIR region. Moreover, the Δn of unstrained MoO_3 is superior to other birefringent materials like KH_2PO_4 [63], $LiNbO_3$ [64] as well as low-symmetry materials such as ReS_2 [23], indicating intrinsic MoO_3 possesses the exceptional birefringent performance. Nevertheless, the Δn of unstrained MoO_3 is lower than that BP [65] in visible region and far below calcite [18] through the visible and NIR region. By applying the −10% *c*-axis strain, however, the Δn of MoO_3 has been tremendously enhanced, which outclasses all the birefringent materials and low-symmetry materials mentioned above.

3.3. *Understanding the strain modulation effect on optically anisotropic and birefringent α-MoO_3*

To understanding the strain modulation effect on optically anisotropic and birefringent α-MoO_3, the band structure of strained α-MoO_3 was firstly calculated to reveal the relation between strain and starting operation wavelength λ_s. Besides, to figure out the connection between strain and birefringence Δn, dipole moment of α-MoO_3 under in-plane strain was also calculated.

Band structure and PDOS of α-MoO_3 under in-plane strain. The band structures of α-MoO_3 under *c*-axis strain, illustrated in Fig. 4a–f, were calculated by hybrid functional of HSE06 method, which is taken as a typical sample to demonstrate E_{CBM} as well as E_{VBM} and bandgap E_g under in-plane strain. Also summed in Table S5, under all the *c*-axis strain, the BZ locations of CBM and VBM remain unchanged, which is still Γ and T point respectively. Moreover, the bandgap E_g under *c*-axis strain linearly descends with the increase of the *c*-axis strain from −10% to 10%. Shown in Fig. 4g and summed in Table S5, compared with the relatively low value and near-zero oscillation of E_{VBM}, the relatively high value and decline tendency make E_{CBM} become a dominate role in determining E_g of Fig. 4h. Band structures under *a*-axis strain have a wide discrepancy with those under *c*-axis strain. First, as displayed in Fig. S16 as well as summed in Table S5, the VBM under −10% and 10% *a*-axis strain no longer locate the T point in BZ, which is similar to the circumstance of the BZ locations of CBM under 5% and 10% *a*-axis tensile strain. Also, though the E_{CBM} plays a leading role in determining E_g in Fig. 4h, the rise of E_{CBM} bring E_g ascending instead of descending like E_{CBM} under *c*-axis strain. The results about E_g under *c*-axis and *a*-axis strain are in keeping with the reported literature [68,69]. For the biaxial strain illustrated in Fig. S17 and summed in Table S5, the VBM's BZ locations are the same as the unstrained α-MoO_3 while BZ locations of CBM under 5% and 10% biaxial tensile strain shift between the Y point and the Γ point. Like the case of the λ_s under biaxial strain, ranges of the E_{CBM} and the E_g under biaxial strain, respectively shown in Fig. 4g and h, are still between those under *a*-axis strain and those under *c*-axis strain, and the E_{CBM} and the E_g are closer to those under *a*-axis strain.

We also discuss the physics behind the change in the E_g under in-plane strain with the help of PDOS under all strained cases in Figs. S18–S20. As mentioned above, the E_{CBM} instead of the E_{VBM} plays a leading role in determining E_g under in-plane strain. As a result, attentions are paid to investigate the variation regular of contributions of carriers from specific atom orbital to E_{CBM} under in-plane strain in PDOS, which is the key to understand the physics behind the change in E_g. As illustrated in Fig. S18, the contributions of carriers from Mo atoms' $4d_{yz}$ orbital gradually decrease and those from Mo atoms' $4d_{xy}$ orbital gradually increase with the increasement of *a*-axis strain from −10% to 10%, leading to the E_{CBM} gradually increasing and thus the increase of E_g under *a*-axis strain. The E_{CBM} as well as E_g, however, is gradually and more linearly decreased with the ascend of *c*-axis percent strain. As shown in Fig. S19, the contributions of carriers in Mo atoms' $4d_{xy}$ orbital gradually decrease rather than increase as the *c*-axis strain rise from −10% to 10%. Therefore, for both *a*-axis and *c*-axis strain, the increasement of the contributions of carriers from Mo atoms' $4d_{xy}$ orbital makes E_{CBM} as well as E_g increase and their decreasement makes E_{CBM} as well as E_g decrease. The E_{CBM} as well as E_g under *a*-axis strain is

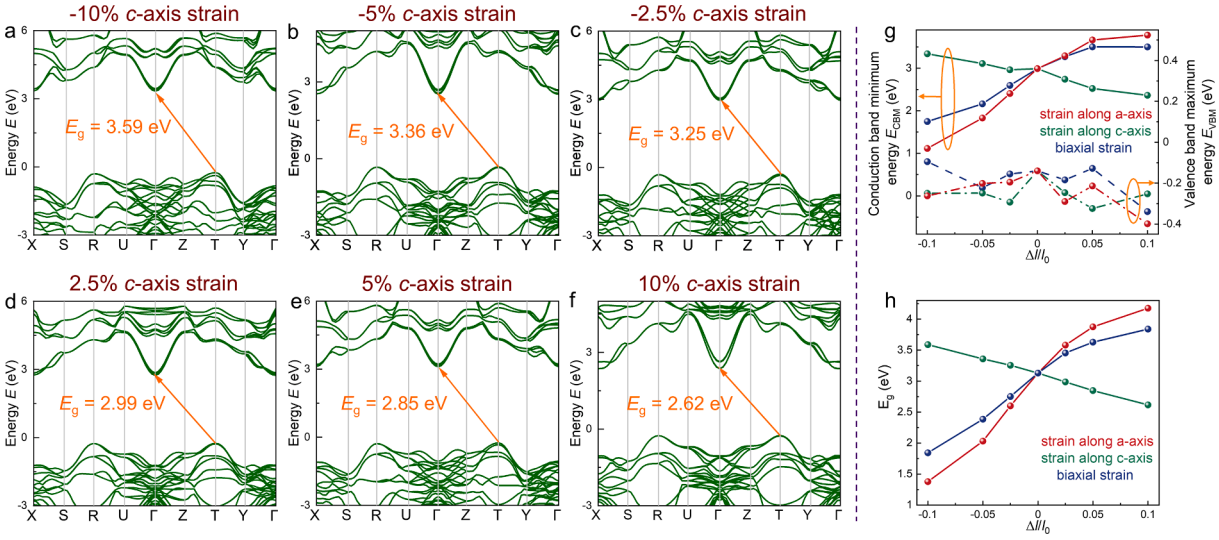

Fig. 4. Band structures of α-MoO_3 under *c*-axis strain (a~f) calculated by hybrid functional of HSE06 method without considering SOC effect. Conduction band minimum (CBM) energy E_{CBM} as well as valence band maximum (VBM) energy E_{VBM} (g) and bandgap E_g (h) under in-plane strain.

influenced by both the contributions of carriers from Mo atoms' $4d_{yz}$ orbital and those from Mo atoms' $4d_{xy}$ orbital. For the E_{CBM} as well as E_g under *c*-axis strain, however, the only variation factor is the contributions of carriers in Mo atoms' $4d_{xy}$ orbital. As a result, the E_{CBM} as well as E_g is more linear with the *c*-axis percent strain. Although affected by the *c*-axis strain, the carriers' contribution behavior of biaxial strain in Fig. S20 are more similar to that of *a*-axis. Therefore, on the one hand, the ranges of the E_{CBM} and the E_g under biaxial strain fall between those of under a-axis strain and those under c-axis strain. On the other hand, the and the E_{CBM} and the E_g are closer to those under *a*-axis strain.

As is known, the energy corresponding to the interband transition usually exceeds the bandgap E_g, and the absorption is often absent below E_g [7,70]. As mentioned before, the starting operation wavelength λ_s is defined when the absorption gradually drop to zero and there is no longer existing any absorption peak. Hence, the λ_s is in possession of a positive relevance to the E_g. To demonstrated their relation, the λ_s is converted to the starting operation energy E_s, by the following relation [59]

$$E_s = 1239.84/\lambda_s, \quad (5)$$

To make the Eq. (5) established, E_s and λ_s need to be the unit of eV and nm, respectively. Demonstrated in Fig. S21, E_s under in-plane strain shares the similar variation trend with E_g under in-plane strain. For the *a*-axis strain, both E_s and E_g increase with the strain rising from −10% to 10%, and E_s also decline with *c*-axis strain ascending, which is like the situation of E_g under *c*-axis strain. Besides, analogous to E_g under biaxial strain, E_s under biaxial strain falls within the range of those under *a*-axis and *c*-axis strain. Above all, we believe that E_g plays a positive and significant role in determining the λ_s under in-plane strain, and thus E_g has a dominate effect on the strain-modulating λ_s. Consequently, the λ_s descending with *a*-axis strain from −10% to 10% is due to the ascendance of E_g within the same range of *a*-axis strain. In contrast, under *c*-axis compressive strain, the λ_s is blue shift and get close to the UV region, which is owing to the fact that the E_g under −10% *c*-axis is highest among those under *c*-axis strain.

Dipole moment of α-MoO_3 under in-plane strain. The calculated dipole moment is composed by ionic part and electronic part, and we often care more about the dipole moment at the center of the crystal cell in unstrained α-MoO_3. It is found that both ionic and electronic dipole moment are zero in unstrained α-MoO_3, which means there is no dipole moment existing in intrinsic α-MoO_3. When applying in-plane strain, however, the unit cell will be changed, illustrated in Fig. 5a and b. As a consequence, the unit cell center of unstrained α-MoO_3 is no more the center of the strained unit cell. Summed in in Table S6, the unstrained unit cell center coordinate value in the corresponding strained unit cell is higher than the unit cell center coordinate value under compressive strain and lower than the unstrained unit cell center coordinate value under tensile strain. As a result, the unstrained unit cell center in the corresponding strained unit cell will contribute the ionic dipole moment, as demonstrated in Fig. 5c and d as well as summed in Table S6. When applying the *a*-axis strain, the ionic dipole moment along −z direction p^{ion}_{-z} falls off with the augment of the strain from −10% to 10% in Fig. 5c, which exhibits the fair similarity with the birefringence Δn under *a*-axis strain. Besides, show in Fig. 5d, the ionic dipole moment along −y direction p^{ion}_{-y} increases linearly with the *c*-axis strain, which is in accordance with the nearly linear growth relation between Δn and the *c*-axis strain.

As mentioned before, anisotropic polarization will give rise to the anisotropic dielectric functions, *i.e.* optical anisotropy [56,59]. Under in-plane strain, in spite of no electronic dipole moment, the ionic dipole moment exists and becomes giant anisotropy. As we know, the sum of the dipole moment p^{ion}_{-l} ($l = x, y, z$) constitutes the polarization P_l ($l = x,$

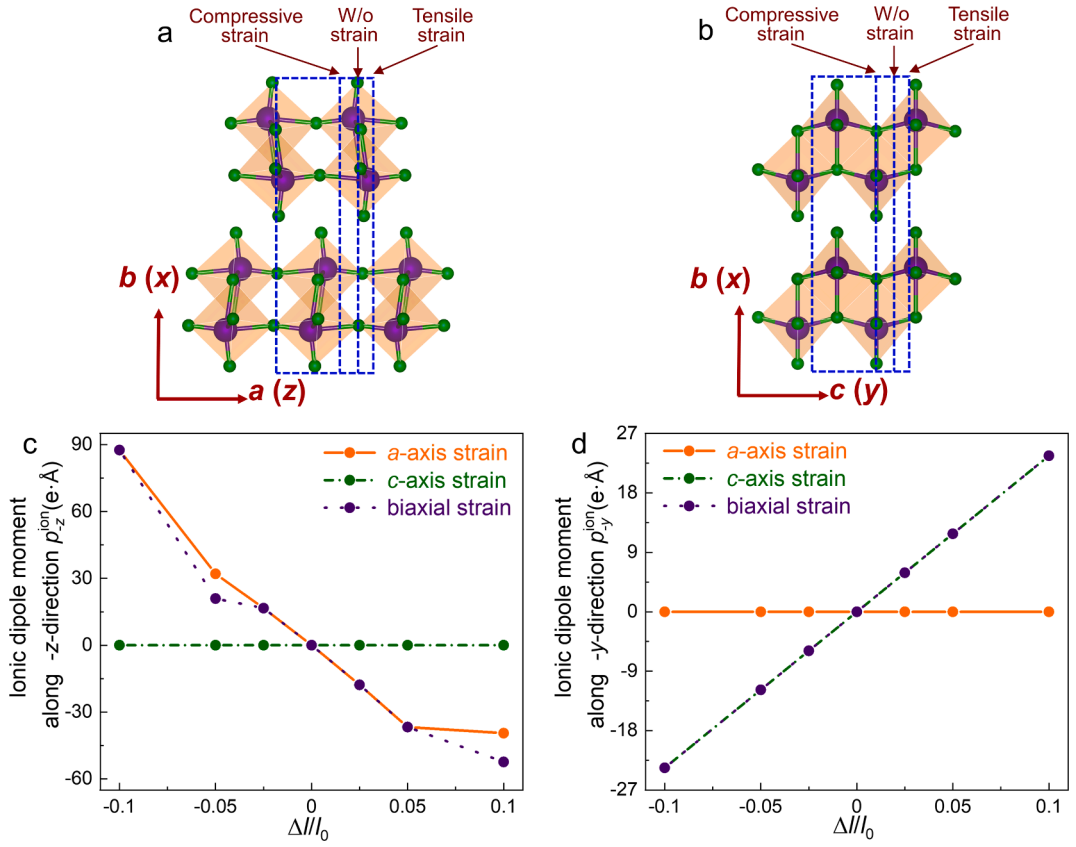

Fig. 5. The unit cell in *x*-*z* plane (a) and *x*-*y* plane (b) under compressive and tensile strain as well as without (w/o) strain with respect to the unstrained α-MoO_3, where *x*-, *y*- and *z*-axis are respectively corresponding to the *b*-, *c*- and *a*-axis of α-MoO_3. Ionic dipole moment along −z direction p^{ion}_{-z} (c) and −y direction p^{ion}_{-y} (d).

y, z), which is [71]

$$P_l = -\sum_m p_{-l}^{\text{ion}},\ l\ =\ x,\ y,\ z. \tag{6}$$

Moreover, the anisotropic polarization P_l ($l = x, y, z$) will lead to the anisotropic dielectric functions ε_l ($l = x, y, z$), according to the following relation [71]

$$\varepsilon_l = 1 + \frac{P_l}{\varepsilon_0 E_l},\ l\ =\ x,\ y,\ z. \tag{7}$$

In Eq. (7), the ε_0 is the dielectric constant in vacuum and E_l ($l = x, y, z$) is the electric field along the x-, y- and z-axis. According to Eqs. (6) and (7) as well as the Eqs. (2) and (3) above, the changing trend of the ionic dipole moment under strain is capable of ultimately reflecting altering tendency of the Δn of strained α-MoO_3. The ionic dipole moments under biaxial strain are identical to or slightly smaller than those under a-axis and c-axis strain. Also, the ionic dipole moments under a-axis strain possess the contrary tendency and sign. As a result, the Δn under biaxial strain falls within the scope of those under a-axis and c-axis strain. Moreover, the enhancement of the Δn under in-plane strain originate from the contribution of the ionic dipole moment under in-plane strain.

4. Conclusions

In conclusions, by applying in-plane strain, α-MoO_3's optical anisotropy and birefringent performance becomes highly tunable and immensely improved, and band structure and dipole moment of strained α-MoO_3 are also calculate to further reveal the strain modulation mechanism. The low-symmetry lattice structure makes intrinsic α-MoO_3 greatly anisotropy in electronics and optics, and we find the unstrained α-MoO_3 is a typically and excellently birefringent material, which is because of not only the visible-region starting operation wavelength λ_s (= 579 nm) but also the relatively high birefringence ($|\Delta n| = 0.105$ @ 1064 nm). The optical anisotropy under in-plane strain is highly tunable. Under a-axis strain, the starting operation wavelength λ_s and the birefringence Δn descend while they ascend under c-axis strain. For the biaxial strain, both the λ_s and the Δn fall within the range of their counterparts under a-axis and c-axis strain. It is also found that the λ_s is extended to approach the UV region by the c-axis compressive strain. More excitingly, the absolute value of birefringence $|\Delta n|$ under −10% c-axis strain is 0.288 at λ_s (= 509 nm), whose percent ratio to that of unstrained α-MoO_3 is as high as 436%. Additionally, $|\Delta k|$ under −10% c-axis strain at λ_s is only 0.005, which is 58.3% lower than that of unstrained α-MoO_3. According to the band structure of strained α-MoO_3, we find that the bandgap energy E_g plays a dominate role in determining strain-modulating λ_s. We also further reveal the physics behind the change in the bandgap E_g under the strained condition with the help of PDOS under all strained cases. Besides, the changing trend of the ionic dipole moment under strain is capable of ultimately reflecting altering tendency of the Δn of strained α-MoO_3, and the enhancement of the Δn under in-plane strain originates from the contribution of the ionic dipole moment under in-plane strain.

We believe that the most possible and facile method to obtain α-MoO_3 under in-plane strain in experiment is to employ the flexible substrate [34], due to the fact that the flexible substrate is capable to supply the uniform in-plane stress studied by this work and the vdW materials like α-MoO_3 can be easily exfoliated onto the such substrate [3]. To be specific, after being exfoliated onto the flexible substrate, the optical anisotropy, quantified by the Δn as well as Δk, can be adjusted and enhanced by applying the uniform in-plane stress to the flexible substrate, accompanied with the α-MoO_3 under in-plane strain. Limited by current experimental conditions especially the strain generation methods, however, most of experimental researches under high strain are within the range of −4%~6% [72–74]. Therefore, more efforts need to be put to realize higher strain applied to the materials to acquire higher performances or novel or potential or even unexpected material properties. Since the α-MoO_3 demonstrates high stability under high percentage (±10%) strain, we believe that α-MoO_3 under such high percentage strain is experimentally possible if the high percentage strain is attainable in experiment. Even adopting current experimental conditions, if −5% c-axis strain is applied to α-MoO_3, according to Table S4, there will be a redshift of only 19 nm in the starting operation wavelength λ_s and the absolute value of the dichroism $|\Delta k|$ will even decrease to 0.002. Also, absolute value of birefringence $|\Delta n|$ under −5% c-axis strain is 0.188 at λ_s, which is still a huge enhancement of 285% compared with the unstrained α-MoO_3.

The strain offers a degree of freedom to regulate α-MoO_3's optical anisotropy and birefringent performance, leading to the corresponding devices based on α-MoO_3 being adjustable. Also, the multiplied-enhancement birefringence can further vastly improve the device performance based on α-MoO_3, such as waveplates, Dyakonov surface waves devices mentioned in introduction section. The proposed calculation method of optical properties under strain as well as strain modulation mechanism in this paper can be utilized and extended to other optically anisotropic and birefringent materials.

CRediT authorship contribution statement

Zhengfeng Guo: Writing – original draft, Visualization, Validation, Methodology, Investigation, Formal analysis, Data curation, Conceptualization. **Jingbo Sun:** Supervision, Resources, Project administration, Funding acquisition. **Ji Zhou:** Supervision, Resources, Project administration. **Honggang Gu:** Writing – review & editing, Supervision, Resources, Project administration, Funding acquisition, Data curation. **Shiyuan Liu:** Supervision, Resources, Project administration, Funding acquisition.

Declaration of competing interest

The authors declare that they have no known competing financial interests or personal relationships that could have appeared to influence the work reported in this paper.

Acknowledgments

This work was funded by the National Key Research and Development Program of China (Grant Nos. 2022YFB3806000 and 2022YFB2803900), the Guangdong Basic and Applied Basic Research Foundation (Grant No. 2023A1515030149), the National Natural Science Foundation of China (Grant No. 52130504), the Key Research and Development Program of Hubei Province (Grant No. 2021BAA013), the Interdisciplinary Research Program of Huazhong University of Science and Technology (HUST) (Grant No. 2023JCYJ047), and the Innovation Project of Optics Valley Laboratory (Grant No. OVL2023PY003).The authors are thankful for the support of the Experiment Center for Advanced Manufacturing and Technology at the School of Mechanical Science & Engineering of HUST, and the Analysis and Testing Center of HUST.

Appendix A. Supplementary data

Calculation parameter settings, comparations between experimental and calculated lattice constants, band structure, PDOS, and anisotropic carrier mobility of α-MoO_3, anisotropic dielectric functions of α-MoO_3, mechanical stability of α-MoO_3, stress–strain relation of α-MoO_3, optical properties of α-MoO_3 under in-plane strain, birefringence Δn under in-plane strain at the wavelength of 1064 nm, band structure and PDOS of strained α-MoO_3, starting operation energy E_s under in-plane strain, and dipole moment of α-MoO_3 under in-plane strain can be found in Supplementary Material. Supplementary data to this article can be found online at https://doi.org/10.1016/j.apsusc.2024.162059.

Data availability

Data will be made available on request.

References

[1] L. Kihlborg, Least squares refinement of crystal structure of molybdenum trioxide, Ark. Kemi 21 (1963) 357–364.
[2] L. Fang, Y. Shu, A. Wang, T. Zhang, Green synthesis and characterization of anisotropic uniform single-crystal α-MoO3 nanostructures, J. Phys. Chem. C 111 (2007) 2401–2408.
[3] W. Ma, P. Alonso-González, S. Li, A.Y. Nikitin, J. Yuan, J. Martín-Sánchez, J. Taboada-Gutiérrez, I. Amenabar, P. Li, S. Vélez, C. Tollan, Z. Dai, Y. Zhang, S. Sriram, K. Kalantar-Zadeh, S.-T. Lee, R. Hillenbrand, Q. Bao, In-plane anisotropic and ultra-low-loss polaritons in a natural van der Waals crystal, Nature 562 (2018) 557–562.
[4] S. Puebla, R. D'Agosta, G. Sanchez-Santolino, R. Frisenda, C. Munuera, A. Castellanos-Gomez, In-plane anisotropic optical and mechanical properties of two-dimensional MoO3, Npj 2D Mater. Appl. 5 (2021) 37.
[5] M. Zhong, K. Zhou, Z. Wei, Y. Li, T. Li, H. Dong, L. Jiang, J. Li, W. Hu, Highly anisotropic solar-blind UV photodetector based on large-size two-dimensional α-MoO3 atomic crystals, 2D Mater. 5 (2018) 035033.
[6] Y. Zhou, Z. Guo, H. Gu, Y. Li, Y. Song, S. Liu, M. Hong, S. Zhao, J. Luo, A solution-processable natural crystal with giant optical anisotropy for efficient manipulation of light polarization, Nat. Photonics 18 (2024) 922–927.
[7] Z. Guo, H. Gu, M. Fang, B. Song, W. Wang, X. Chen, C. Zhang, H. Jiang, L. Wang, S. Liu, Complete dielectric tensor and giant optical anisotropy in quasi-one-dimensional ZrTe5, ACS Mater. Lett. 3 (2021) 525–534.
[8] J. Qiao, X. Kong, Z.-X. Hu, F. Yang, W. Ji, High-mobility transport anisotropy and linear dichroism in few-layer black phosphorus, Nat. Commun. 5 (2014) 4475.
[9] Z. Guo, H. Gu, Y. Yu, Q. Zhang, Z. Wei, S. Liu, Wavelength-linearly-dependent and polarization-sensitive perfect absorbers based on optically anisotropic germanium selenide (GeSe), Adv. Opt. Mater. 12 (2024) 2303138.
[10] N.R. Sahoo, S. Dixit, A.K. Singh, S.H. Nam, N.X. Fang, A. Kumar, High temperature Mid-IR polarizer via natural in-plane hyperbolic van der waals crystals, Adv. Opt. Mater. 10 (2022) 2101919.
[11] S. Abedini Dereshgi, T.G. Folland, A.A. Murthy, X. Song, I. Tanriover, V.P. Dravid, J.D. Caldwell, K. Aydin, Lithography-free IR polarization converters via orthogonal in-plane phonons in α-MoO3 flakes, Nat. Commun. 11 (2020) 5771.
[12] X. Hu, K. Liu, Y. Cai, S.-Q. Zang, T. Zhai, 2D oxides for electronics and optoelectronics, Small Sci. 2 (2022) 2200008.
[13] M. Coll, J. Fontcuberta, M. Althammer, M. Bibes, H. Boschker, A. Calleja, G. Cheng, M. Cuoco, R. Dittmann, B. Dkhil, I. El Baggari, M. Fanciulli, I. Fina, E. Fortunato, C. Frontera, S. Fujita, V. Garcia, S.T.B. Goennenwein, C.G. Granqvist, J. Grollier, R. Gross, A. Hagfeldt, G. Herranz, K. Hono, E. Houwman, M. Huijben, A. Kalaboukhov, D.J. Keeble, G. Koster, L.F. Kourkoutis, J. Levy, M. Lira-Cantu, J. L. MacManus-Driscoll, J. Mannhart, R. Martins, S. Menzel, T. Mikolajick, M. Napari, M.D. Nguyen, G. Niklasson, C. Paillard, S. Panigrahi, G. Rijnders, F. Sánchez, P. Sanchis, S. Sanna, D.G. Schlom, U. Schroeder, K.M. Shen, A. Siemon, M. Spreitzer, H. Sukegawa, R. Tamayo, J. van den Brink, N. Pryds, F.M. Granozio, Towards oxide electronics: A roadmap, Appl. Surf. Sci. 482 (2019) 1–93.
[14] S. Balendhran, J. Deng, J.Z. Ou, S. Walia, J. Scott, J. Tang, K.L. Wang, M.R. Field, S. Russo, S. Zhuiykov, M.S. Strano, N. Medhekar, S. Sriram, M. Bhaskaran, K. Kalantar-zadeh, Enhanced charge carrier mobility in two-dimensional high dielectric molybdenum oxide, Adv. Mater. 25 (2013) 109–114.
[15] L. Cheng, M. Shao, X. Wang, H. Hu, Single-crystalline molybdenum trioxide nanoribbons: photocatalytic, photoconductive, and electrochemical properties, Chem. - Eur. J. 15 (2009) 2310–2316.
[16] E. Pavoni, M.G. Modreanu, E. Mohebbi, D. Mencarelli, P. Stipa, E. Laudadio, L. Pierantoni, First-principles calculation of MoO2 and MoO3 electronic and optical properties compared with experimental data, Nanomaterials 13 (2023) 1319.
[17] M. Shahrokhi, P. Raybaud, T. Le Bahers, On the understanding of the optoelectronic properties of S-doped MoO3 and O-doped MoS2 bulk systems: A DFT perspective, J. Mater. Chem. C 8 (2020) 9064–9074.
[18] G. Ghosh, Dispersion-equation coefficients for the refractive index and birefringence of calcite and quartz crystals, Opt. Commun. 163 (1999) 95–102.
[19] M.J. Dodge, Refractive properties of magnesium fluoride, Appl. Opt. 23 (1984) 1980–1985.
[20] S. Abedini Dereshgi, Y.-S. Lee, M.C. Larciprete, M. Centini, V.P. Dravid, K. Aydin, Low-symmetry α-MoO3 heterostructures for wave plate applications in visible frequencies, Adv. Opt. Mater. 11 (2023) 2202603.
[21] C. Wei, S. Abedini Dereshgi, X. Song, A. Murthy, V.P. Dravid, T. Cao, K. Aydin, Polarization reflector/color filter at visible frequencies via anisotropic α-MoO3, Adv. Opt. Mater. 8 (2020) 2000088.
[22] Z. Li, X. Ma, F. Wei, D. Wang, Z. Deng, M. Jiang, A. Siddiquee, K. Qi, D. Zhu, M. Zhao, M. Shen, P. Canepa, S. Kou, J. Lin, Q. Wang, As-grown miniaturized true zero-order waveplates based on low-dimensional ferrocene crystals, Adv. Mater. 35 (2023) 2302468.
[23] H. Yang, H. Jussila, A. Autere, H.-P. Komsa, G. Ye, X. Chen, T. Hasan, Z. Sun, Optical waveplates based on birefringence of anisotropic two-dimensional layered materials, ACS Photonics 4 (2017) 3023–3030.
[24] O. Takayama, D. Artigas, L. Torner, Lossless directional guiding of light in dielectric nanosheets using Dyakonov surface waves, Nat. Nanotechnol. 9 (2014) 419–424.
[25] Y. Li, J. Sun, Y. Wen, J. Zhou, Controllable selective coupling of dyakonov surface waves at a liquid-crystal-based interface, Phys. Rev. Appl. 13 (2020) 024024.
[26] X. Chen, W.-G. Lu, J. Tang, Y. Zhang, Y. Wang, G.D. Scholes, H. Zhong, Solution-processed inorganic perovskite crystals as achromatic quarter-wave plates, Nat. Photonics 15 (2021) 813–816.
[27] O. Takayama, L.-C. Crasovan, S.K. Johansen, D. Mihalache, D. Artigas, L. Torner, Dyakonov surface waves: A review, Electromagnetics 28 (2008) 126–145.
[28] M. Fang, H. Gu, Z. Guo, J. Liu, L. Huang, S. Liu, Temperature and thickness dependent dielectric functions of MoTe2 thin films investigated by spectroscopic ellipsometry, Appl. Surf. Sci. 605 (2022) 154813.
[29] T. Zheng, M. Runowski, J. Xue, L. Luo, U.R. Rodríguez-Mendoza, V. Lavín, I. R. Martín, P. Rodríguez-Hernández, A. Muñoz, P. Du, Giant pressure-induced spectral shift in cyan-emitting Eu2+-Activated Sr8Si4O12Cl8 microspheres for ultrasensitive visual manometry, Adv. Funct. Mater. 33 (2023) 2214663.
[30] V. Christiansson, F. Petocchi, P. Werner, Correlated electronic structure of $La_3Ni_2O_7$ under pressure, Phys. Rev. Lett. 131 (2023) 206501.
[31] Z. Zhou, R. Song, J. Xu, X. Ni, Z. Dang, Z. Zhao, J. Quan, S. Dong, W. Hu, D. Huang, K. Chen, Z. Wang, X. Cheng, M.B. Raschke, A. Alù, T. Jiang, Gate-tuning hybrid polaritons in twisted α-MoO3/graphene heterostructures, Nano Lett. 23 (2023) 11252–11259.
[32] F. Dirnberger, J. Quan, R. Bushati, G.M. Diederich, M. Florian, J. Klein, K. Mosina, Z. Sofer, X. Xu, A. Kamra, F.J. García-Vidal, A. Alù, V.M. Menon, Magneto-optics in a van der Waals magnet tuned by self-hybridized polaritons, Nature 620 (2023) 533–537.
[33] S. Biswas, M.Y. Grajower, K. Watanabe, T. Taniguchi, H.A. Atwater, Broadband electro-optic polarization conversion with atomically thin black phosphorus, Science 374 (2021) 448–453.
[34] A. Castellanos-Gomez, R. Roldán, E. Cappelluti, M. Buscema, F. Guinea, H.S.J. van der Zant, G.A. Steele, Local strain engineering in atomically thin MoS2, Nano Lett 13 (2013) 5361–5366.
[35] C. Martella, C. Mennucci, E. Cinquanta, A. Lamperti, E. Cappelluti, F. Buatier de Mongeot, A. Molle, Anisotropic MoS2 nanosheets grown on self-organized nanopatterned substrates, Adv. Mater. 29 (2017) 1605785.
[36] C. Zhang, M.-Y. Li, J. Tersoff, Y. Han, Y. Su, L.-J. Li, D.A. Muller, C.-K. Shih, Strain distributions and their influence on electronic structures of WSe2–MoS2 laterally strained heterojunctions, Nat. Nanotechnol. 13 (2018) 152–158.
[37] Z. Liu, M. Amani, S. Najmaei, Q. Xu, X. Zou, W. Zhou, T. Yu, C. Qiu, A.G. Birdwell, F.J. Crowne, R. Vajtai, B.I. Yakobson, Z. Xia, M. Dubey, P.M. Ajayan, J. Lou, Strain and structure heterogeneity in MoS2 atomic layers grown by chemical vapour deposition, Nat. Commun. 5 (2014) 5246.
[38] M.G. Harats, J.N. Kirchhof, M. Qiao, K. Greben, K.I. Bolotin, Dynamics and efficient conversion of excitons to trions in non-uniformly strained monolayer WS2, Nat. Photonics 14 (2020) 324–329.
[39] S. Manzeli, A. Allain, A. Ghadimi, A. Kis, Piezoresistivity and strain-induced band gap tuning in atomically thin moS2, Nano Lett. 15 (2015) 5330–5335.
[40] E. Blundo, E. Cappelluti, M. Felici, G. Pettinari, A. Polimeni, Strain-tuning of the electronic, optical, and vibrational properties of two-dimensional crystals, Appl. Phys. Rev. 8 (2021).
[41] Y. Qi, M.A. Sadi, D. Hu, M. Zheng, Z. Wu, Y. Jiang, Y.P. Chen, Recent progress in strain engineering on Van der Waals 2D materials: Tunable electrical, electrochemical, magnetic, and optical properties, Adv. Mater. 35 (2023) 2205714.
[42] H. Li, A.W. Contryman, X. Qian, S.M. Ardakani, Y. Gong, X. Wang, J.M. Weisse, C. H. Lee, J. Zhao, P.M. Ajayan, J. Li, H.C. Manoharan, X. Zheng, Optoelectronic crystal of artificial atoms in strain-textured molybdenum disulphide, Nat. Commun. 6 (2015) 7381.
[43] Z. Li, Y. Lv, L. Ren, J. Li, L. Kong, Y. Zeng, Q. Tao, R. Wu, H. Ma, B. Zhao, D. Wang, W. Dang, K. Chen, L. Liao, X. Duan, X. Duan, Y. Liu, Efficient strain modulation of 2D materials via polymer encapsulation, Nat. Commun. 11 (2020) 1151.
[44] Z. Zhang, W. Wang, Y. Jiang, Y.-X. Wang, Y. Wu, J.-C. Lai, S. Niu, C. Xu, C.-C. Shih, C. Wang, H. Yan, L. Galuska, N. Prine, H.-C. Wu, D. Zhong, G. Chen, N. Matsuhisa, Y. Zheng, Z. Yu, Y. Wang, R. Dauskardt, X. Gu, J.B.H. Tok, Z. Bao, High-brightness all-polymer stretchable LED with charge-trapping dilution, Nature 603 (2022) 624–630.
[45] T. Niu, Q. Meng, D. Zhou, N. Si, S. Zhai, X. Hao, M. Zhou, H. Fuchs, Large-scale synthesis of strain-tunable semiconducting antimonene on copper oxide, Adv. Mater. 32 (2020) 1906873.
[46] H. Kim, S.Z. Uddin, D.-H. Lien, M. Yeh, N.S. Azar, S. Balendhran, T. Kim, N. Gupta, Y. Rho, C.P. Grigoropoulos, K.B. Crozier, A. Javey, Actively variable-spectrum optoelectronics with black phosphorus, Nature 596 (2021) 232–237.
[47] B.S. Dandogbessi, O. Akin-Ojo, First principles prediction of the electronic structure and carrier mobilities of biaxially strained molybdenum trioxide (MoO3), J. Appl. Phys. 120 (2016).
[48] G. Kresse, J. Furthmüller, Efficiency of ab-initio total energy calculations for metals and semiconductors using a plane-wave basis set, Comput. Mater. Sci. 6 (1996) 15–50.
[49] J.P. Perdew, K. Burke, M. Ernzerhof, Generalized gradient approximation made simple, Phys. Rev. Lett. 77 (1996) 3865–3868.
[50] J. Heyd, G.E. Scuseria, M. Ernzerhof, Hybrid functionals based on a screened Coulomb potential, J. Chem. Phys. 118 (2003) 8207–8215.
[51] M. Kim, W.J. Kim, E.K. Lee, S. Lebègue, H. Kim, Recent development of atom-pairwise van der waals corrections for density functional theory: From molecules to solids, Int. J. Quantum Chem. 116 (2016) 598–607.
[52] S. Grimme, Semiempirical GGA-type density functional constructed with a long-range dispersion correction, J. Comput. Chem. 27 (2006) 1787–1799.
[53] Y.-P. Zhu, X. Chen, X.-R. Liu, Y. Liu, P. Liu, H. Zha, G. Qu, C. Hong, J. Li, Z. Jiang, X.-M. Ma, Y.-J. Hao, M.-Y. Zhu, W. Liu, M. Zeng, S. Jayaram, M. Lenger, J. Ding,

S. Mo, K. Tanaka, M. Arita, Z. Liu, M. Ye, D. Shen, J. Wrachtrup, Y. Huang, R.-H. He, S. Qiao, Q. Liu, C. Liu, Observation of plaid-like spin splitting in a noncoplanar antiferromagnet, Nature 626 (2024) 523–528.
[54] M.K. Jana, R. Song, Y. Xie, R. Zhao, P.C. Sercel, V. Blum, D.B. Mitzi, Structural descriptor for enhanced spin-splitting in 2D hybrid perovskites, Nat. Commun. 12 (2021) 4982.
[55] L.D. Whalley, J.M. Frost, B.J. Morgan, A. Walsh, Impact of nonparabolic electronic band structure on the optical and transport properties of photovoltaic materials, Phys. Rev. B 99 (2019) 085207.
[56] Z. Guo, H. Gu, M. Fang, L. Ye, S. Liu, Giant in-plane optical and electronic anisotropy of tellurene: a quantitative exploration, Nanoscale 14 (2022) 12238–12246.
[57] A.M. Ganose, J. Park, A. Faghaninia, R. Woods-Robinson, K.A. Persson, A. Jain, Efficient calculation of carrier scattering rates from first principles, Nat. Commun. 12 (2021) 2222.
[58] K. Wang, Y. Shen, X. Meng, L. Lv, Y. Zhang, X. Yang, M. Zhou, N. Zhang, Q. He, B. Zhang, Z. Zhou, High stability and tunable hydrogen evolution material with defect-enhanced photocatalytic properties:penta-BAs5 monolayer, Vacuum 221 (2024) 112904.
[59] H. Fujiwara, Spectroscopic ellipsometry: Principles and applications, John Wiley & Sons, Chichester, England, 2007.
[60] Z. Guo, H. Gu, Y. Yu, Z. Wei, S. Liu, Broadband and incident-angle-modulation near-infrared polarizers based on optically anisotropic SnSe, Nanomaterials 13 (2023) 134.
[61] H. Kolsky, An Investigation of the Mechanical Properties of Materials at very High Rates of Loading, Proc. Phys. Soc. B 62 (1949) 676.
[62] W.Y. Ching, P. Rulis, A. Misra, Ab initio elastic properties and tensile strength of crystalline hydroxyapatite, Acta Biomater. 5 (2009) 3067–3075.
[63] F. Zernike, Refractive indices of ammonium dihydrogen phosphate and potassium dihydrogen phosphate between 2000 Å and 1.5 μ,, J. Opt. Soc. Am. 54 (1964) 1215–1220.
[64] D.F. Nelson, R.M. Mikulyak, Refractive indices of congruently melting lithium niobate, J. Appl. Phys. 45 (1974) 3688–3689.
[65] S.-Y. Lee, K.-J. Yee, Black phosphorus phase retarder based on anisotropic refractive index dispersion, 2D Mater. 9 (2021) 015020.
[66] Q. Liang, Q. Wang, Q. Zhang, J. Wei, S.X. Lim, R. Zhu, J. Hu, W. Wei, C. Lee, C. Sow, W. Zhang, A.T.S. Wee, High-performance, room temperature, ultra-broadband photodetectors based on air-stable PdSe2, Adv. Mater. 31 (2019) 1807609.
[67] T. Sugiyama, K.-I. Yuyama, H. Masuhara, Laser trapping chemistry: from polymer assembly to amino acid crystallization, Acc. Chem. Res. 45 (2012) 1946–1954.
[68] F. Li, Z. Chen, Tuning electronic and magnetic properties of MoO3 sheets by cutting, hydrogenation, and external strain: a computational investigation, Nanoscale 5 (2013) 5321–5333.
[69] P.-R. Huang, Y. He, C. Cao, Z.-H. Lu, Impact of lattice distortion and electron doping on α-MoO3 electronic structure, Sci. Rep. 4 (2014) 7131.
[70] H. Gu, B. Song, M. Fang, Y. Hong, X. Chen, H. Jiang, W. Ren, S. Liu, Layer-dependent dielectric and optical properties of centimeter-scale 2D WSe2: evolution from a single layer to few layers, Nanoscale 11 (2019) 22762–22771.
[71] M. Brinkmann, J. Hayden, M. Letz, S. Reichel, C. Click, W. Mannstadt, B. Schreder, S. Wolff, S. Ritter, M.J. Davis, T.E. Bauer, H. Ren, Y.-H. Fan, Y. Menke, S.-T. Wu, K. Bonrad, E. Krätzig, K. Buse, R.A. Paquin, Optical materials and their properties, in: F. Träger (Ed.), Springer Handbook of Lasers and Optics, Springer, Berlin Heidelberg, Berlin, Heidelberg, 2012, pp. 253–399.
[72] Z. Huangfu, J. Wang, X. Cheng, S. Feng, Y. Liang, C. Yuan, X. Zhu, Z. Wang, H. Zhang, K. Yang, The effect of different strain on the structural and optical properties of multilayer γ-InSe, J. Alloys Compd. 961 (2023) 170998.
[73] Y. Sun, Z. Liu, Z. Li, F. Qin, J. Huang, C. Qiu, H. Yuan, Unravelling the anisotropic light-matter interaction in strain-engineered trihalide MoCl3, Nano Res. 17 (2024) 2981–2987.
[74] K. Tokár, J. Brndiar, I. Štich, Raman activity of multilayer phosphorene under strain, ACS Omega 4 (2019) 22418–22425.